

Cite this: *Chem. Sci.*, 2022, 13, 9560

All publication charges for this article have been paid for by the Royal Society of Chemistry

Biomimetic catalytic aerobic oxidation of C–sp(3)–H bonds under mild conditions using galactose oxidase model compound Cu^{II}L[†]

Xiao-Hui Liu,^a Hai-Yang Yu,^a Jia-Ying Huang,^a Ji-Hu Su,^c Can Xue,^{ID a}
Xian-Tai Zhou,^{ID *a} Yao-Rong He,^b Qian He,^{ID b} De-Jing Xu,^a Chao Xiong^b
and Hong-Bing Ji^{ID *b}

Developing highly efficient catalytic protocols for C–sp(3)–H bond aerobic oxidation under mild conditions is a long-desired goal of chemists. Inspired by nature, a biomimetic approach for the aerobic oxidation of C–sp(3)–H by galactose oxidase model compound Cu^{II}L and NHPI (*N*-hydroxyphthalimide) was developed. The Cu^{II}L–NHPI system exhibited excellent performance in the oxidation of C–sp(3)–H bonds to ketones, especially for light alkanes. The biomimetic catalytic protocol had a broad substrate scope. Mechanistic studies revealed that the Cu^I-radical intermediate species generated from the intramolecular redox process of Cu^{II}LH₂ was critical for O₂ activation. Kinetic experiments showed that the activation of NHPI was the rate-determining step. Furthermore, activation of NHPI in the Cu^{II}L–NHPI system was demonstrated by time-resolved EPR results. The persistent PINO (phthalimide-*N*-oxyl) radical mechanism for the aerobic oxidation of C–sp(3)–H bond was demonstrated.

Received 10th May 2022

Accepted 28th July 2022

DOI: 10.1039/d2sc02606f

rsc.li/chemical-science

Introduction

Oxidation is one of the most useful chemical transformations in organic synthesis and the modern chemical industry.¹ Oxidation of the C–sp(3)–H bond is extremely challenging due to the high bond energy of the C–H bond.² Various catalysts have been used for the conversion of hydrocarbons, ranging from heterogeneous³ to homogeneous catalytic systems,⁴ as well as bio- and enzymatic catalysts.⁵ In heterogeneous catalytic systems, alkanes are usually first converted to more active alkenes *via* oxidative dehydrogenation.⁶ To achieve acceptable conversion and selectivity, these processes are often carried out under harsh conditions (*e.g.*, high temperatures 500–900 °C).⁷ In the presence of O₂ or other peroxide oxidants, C–H bonds could be oxyfunctionalized by transition metals in homogeneous catalytic systems.^{1a} Usually, assistance of light,⁸ electricity,⁹ or other additives¹⁰ is necessary. Therefore, a more sustainable and environmentally benign oxidative protocol for the chemical conversion of hydrocarbons is desirable.

Copper-containing metalloprotein galactose oxidase (GO) is an enzyme which selectively catalyzes the aerobic oxidation of alcohols to aldehydes under mild conditions.¹¹ From the structure, it could be known that GOase contains two one-electron redox centers, a mononuclear copper center and a tyrosyl radical ligand (Tyr 272).¹² The Tyr 272 radical ligand in GOase abstracts H from the α -carbon of alcoholate and undergoes intramolecular electron transfer to form aldehyde and a Cu^I species. Finally, the reduced GOase is converted to its original form by O₂ along with the formation of 1 equiv. of H₂O₂ (Scheme 1A).¹³

In the past, some GOase model compounds have been synthesized by employing redox-active non-innocent ligands (Scheme 1B).¹⁴ Kitajima reported a salen type copper(II) complex as a possible GOase model.¹⁵ Stack¹⁶ and Pierre's¹⁷ functional models were developed. Subsequently, a mononuclear Cu^{II}–phenoxyl complex was synthesized by Chaudhuri and Wieghardt.^{13a,18} These model compounds are capable of oxidizing primary/secondary alcohols to the corresponding ketones in the presence of O₂. However, GOase has insufficient activity to oxidize hydrocarbons due to the high BDE (bond dissociation energy) of the C–H bond in most hydrocarbons (85–105 kcal mol^{−1}).^{2b,19}

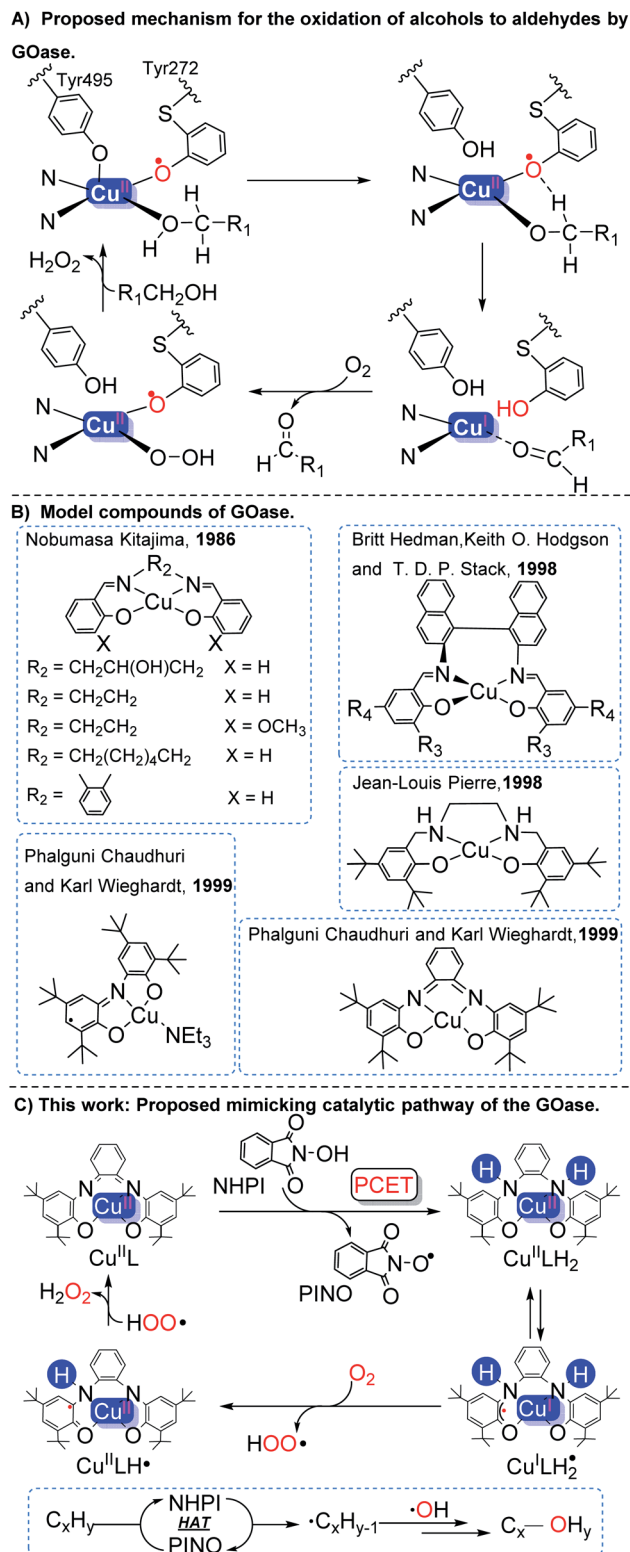
N-Hydroxyphthalimide (NHPI) is an efficient and low-cost *N*-oxyl precursor capable of producing a highly active phthalimide-*N*-oxyl (PINO) radical, which is widely used in the aerobic oxidation of hydrocarbons.²⁰ Ishii and co-workers innovatively introduced metal salts and NHPI for the oxidation reaction of isobutane with molecular oxygen (100 °C).²¹ Jiao and co-workers

^aFine Chemical Industry Research Institute, School of Chemical Engineering and Technology, Sun Yat-sen University, Zhuhai, 519082, China. E-mail: zhouxtai@mail.sysu.edu.cn

^bFine Chemical Industry Research Institute, School of Chemistry, Sun Yat-sen University, Guangzhou 510275, China. E-mail: jihb@mail.sysu.edu.cn

^cCAS Key Laboratory of Microscale Magnetic Resonance, University of Science and Technology of China, Hefei 230026, China. E-mail: sujihu@ustc.edu.cn

[†] Electronic supplementary information (ESI) available. See <https://doi.org/10.1039/d2sc02606f>



Scheme 1 (A) Proposed mechanism for the oxidation of alcohols to aldehydes by GOase. (B) Model compounds of GOase. (C) This work.

developed $\text{PdCl}_2/\text{NHPI}$ for C–sp(2)–H hydroxylation (100 °C).²² However, PINO readily self-decomposes at high temperature (>80 °C) and under alkaline conditions.^{19a,23} In addition, the application of NHPI was restricted because of the long initiation

period and short existence time of PINO.^{20d} In response to these challenges, an electrochemical pathway was developed to activate NHPI under mild conditions by Jensen and co-workers.²⁴ Wang described the approach of PINO radical generation through the irradiation of $\alpha\text{-Fe}_2\text{O}_3$ and NHPI using 455 nm light.²⁵ It has also been reported that ionic liquids²⁶ and fluorine-containing solutions²⁷ were utilized to stabilize PINO.

Inspired by the structure of galactose oxidase, the oxidation protocol of the C–sp(3)–H bond was developed, in which the $\text{Cu}^{\text{II}}\text{L}$ catalyst (ligand: *N,N*-bis(3,5-di-*tert*-butyl-2-hydroxyphenyl)-1,2-phenylenediamine)¹⁸ and NHPI were introduced. Through the proton coupling electron transfer (PCET) process, two electrons and protons were transferred from NHPI to $\text{Cu}^{\text{II}}\text{L}$ to form $\text{Cu}^{\text{II}}\text{LH}_2$ and the PINO radical. The PINO radical can abstract H from the C–H bond of the substrate to produce a high-activity carbon-centered radical through hydrogen atom transformation (HAT). Subsequently, *in situ* generated $\text{Cu}^{\text{II}}\text{LH}_2$ reacts with O_2 to produce H_2O_2 and $\text{Cu}^{\text{II}}\text{L}$ (Scheme 1C). In addition, the detailed mechanism was investigated with the assistance of *in situ* UV-vis spectroscopy, electron paramagnetic resonance (EPR) spectroscopy, X-ray absorption near-edge structure (XANES), as well as thermodynamic and kinetic analysis combined with density functional theory (DFT).

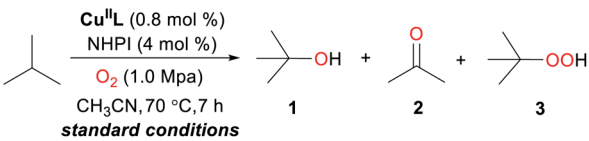
Results and discussion

We initiated aerobic oxidation of the C–sp(3)–H bond by using isobutane as a model substrate (Table 1). After an extensive survey of reaction conditions, including the amount of catalyst ($\text{Cu}^{\text{II}}\text{L}$) (Fig. S1†), the amount of NHPI (Fig. S2†) and reaction temperature (Fig. S3†), the optimized conditions were obtained (isobutane 21 mmol, O_2 1.0 MPa, 70 °C, $\text{Cu}^{\text{II}}\text{L}$ 0.8 mol%, NHPI 4.0 mol%, CH_3CN solvent 20 mL). Under the optimized conditions, isobutane conversion was up to 75%, and the desired hydroxylation product *tert*-butanol (**1**) was obtained in 80% selectivity (Table 1, entry 1).

The control experiments indicated that $\text{Cu}^{\text{II}}\text{L}$ and NHPI were indispensable for the success of this oxidation. Especially, the selectivity of *tert*-butanol was closely related to $\text{Cu}^{\text{II}}\text{L}$ or NHPI (Table 1, entries 2 and 3). When using other Cu-based catalysts such as CuCl_2 and CuCl , a lower yield of **1** and conversion of isobutane was observed (Table 1, entries 4 and 5). The results of solvent screening showed that CH_3CN was the optimal solvent for this reaction (Table 1, entries 6 and 7). Surprisingly, when the oxidation was conducted in air (2.0 MPa), the selectivity of **1** increased (84%) and the conversion slightly decreased (68%) (Table 1, entry 8). Gratifyingly, after 5 cycles of the reaction, the catalytic system still showed excellent catalytic activity (Fig. S4†). Poor efficiency and selectivity were obtained when using the typical $\text{Co}(\text{OAc})_2/\text{NHPI}$ as the catalyst under the same conditions as previously reported²¹ (Table 1, entry 9). Addition of butylated hydroxytoluene (BHT, radical scavenger) resulted in oxidation being completely suppressed (Table 1, entry 10).

With the optimal reaction conditions in hand, the scope of hydrocarbons was subsequently explored. Indane and 1,2,3,4-tetrahydronaphthalene were oxidized to the corresponding ketones in remarkable conversion (99%) and selectivity (99%)

Table 1 Optimization of reaction conditions^a

					
Entry	Deviation from the standard conditions	Conv. (%)	Selectivities ^b (%)		
			1	2	3
1	None	75	80	20	0
2	Without Cu ^{II} L	4	24	16	60
3	Without NHPI	10	39	62	0
4	CuCl ₂ (0.8 mol%) instead of Cu ^{II} L	45	78	22	0
5	CuCl (0.8 mol%) instead of Cu ^{II} L	29	72	28	0
6	Dichloroethane as a solvent	23	21	24	55
7	DMF as a solvent	33	74	17	9
8	Air (2.0 MPa) instead of O ₂	68	84	16	0
9	Co(OAc) ₂ ·4H ₂ O (0.8 mol%) instead of Cu ^{II} L	26	60	12	28
10	BHT (10 mol%) as a radical scavenger	n.r.	—	—	—

^a Standard conditions: isobutane (21 mmol), Cu^{II}L (0.8 mol%), CH₃CN (20 mL), O₂ (1.0 MPa), 70 °C, 7 h. ^b Determined by GC with naphthalene as the internal standard. n.r. = no reaction, "—" means no detection.

(Table 2, entries 1 and 2). In addition, ethylbenzene was transformed into acetophenone in excellent selectivity (97%) (Table 2, entry 3). Meanwhile, toluene was oxidized to benzaldehyde (24%) and benzoic acid (76%) (Table 2, entry 4).

The effect of steric hindrance was observed from the oxidation of propylbenzene and dphenylmethane (Table 2, entries 5 and 6). Cyclopentane was oxidized to cyclopentanone with 83% selectivity and cyclopentanol (17% selectivity) (Table 2, entry 7). For cyclohexene containing both C–sp(3)–H and C=C bonds, the total selectivity of C–sp(3)–H bond oxidation to alcohols and ketones was 83%, and the selectivity of epoxide was 17% (Table 2, entry 8). It indicated that the biomimetic catalytic system exhibited high regioselectivity.

Surprisingly, the quite inert ethane (C–H BDE: 101.1 kcal mol^{−1})²⁸ could be oxidized to acetaldehyde (24%) and acetic acid (76%) at 100 °C (Table 2, entry 9). Heartened by this result, we also conducted experiments on the oxidation of propane. Propane was oxidized to acetone with satisfactory conversion (34%) and 93% selectivity (Table 2, entry 10). Moreover, *n*-butane was smoothly oxidized to methyl ethyl ketone (MEK) with 66% conversion and 66% selectivity (Table 2, entry 11).

To gain insight into the reaction pathway, the reaction between Cu^{II}L and NHPI was originally investigated. The X-band EPR spectrum of the nearly square-planar (*D*_{4h}) Cu^{II}L in CH₃CN recorded at 90 K displayed a typical Cu(II) signal with an unpaired electron in the *d*_{x²−y² orbital (Fig. S5†).²⁹ From the optimal geometric configuration of Cu^{II}L (B3LYP/6-31G(d,p)/IEF-PCM (solvent model) level with CH₃CN as a solvent), the *d*_{x²−y² orbital of the central Cu(II) atom was perpendicular to the π orbitals in the aromatic ring (Fig. S6†). This orbital orientation minimized the spatial overlap between the orthogonal}}

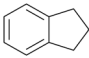
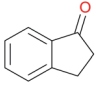
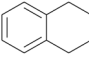
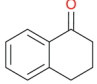
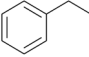
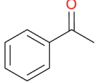
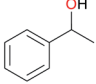
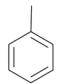
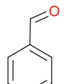
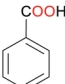
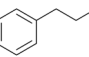
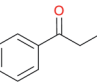
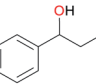
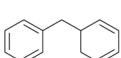
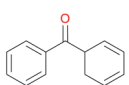
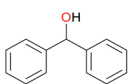
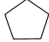
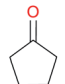
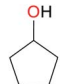
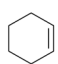
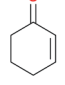
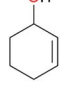
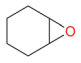

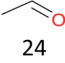
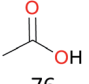
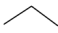
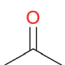
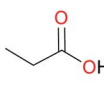
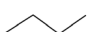
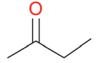
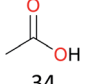
*d*_{x²−y² orbital of Cu(II) and the ligand's π orbitals, resulting in a difficulty for ligand to metal Cu(II) charge transfer (LMCT) to occur.³⁰}

Cu^{II}L has characteristic bands at 435 nm and 1167 nm with a black-green color in CH₃CN solution (Fig. 1A, orange line). To determine the type of absorption peak, the electronic UV-vis-NIR absorption spectra of Cu^{II}L were recorded using the TD-B3LYP/6-31G(d,p) method and IEF-PCM solvent model for CH₃CN. The obtained absorption spectra, the FMO pictures, and the vertical excitation energies are given in Fig. S6†, S7 and Table S1,† respectively. The obtained peaks at 435 nm (calcd. λ = 529 nm, f = 0.0581) and 1167 nm (calcd. λ = 1022 nm, f = 0.1249) of Cu^{II}L were attributed to β -SOMO (the highest singly occupied molecular orbital)-4 to β -SUMO (the lowest singly unoccupied molecular orbital) and β -SOMO-1 to β -SUMO transitions, respectively. These are mainly intraligand charge-transfer (ILCT) transitions.³¹ Another intense band of Cu^{II}L in the UV region (<380 nm) was attributed to the π to π^* transition within the ligand's aromatic ring (α -SOMO to α -SUMO+2, calcd. λ = 364 nm, f = 0.2001).³² It indicates that it is difficult for an intramolecular redox reaction to occur in planar structured Cu^{II}L.

As shown in the cyclic voltammograms (Fig. S9†), the Cu^{II}L complex in CH₃CN showed two reversible oxidations ($E_{1/2}^{\text{ox1}}$ = −0.17 V and $E_{1/2}^{\text{ox2}}$ = 0.30 V vs. Fc^{+/0}, the same below) and two reversible reductions ($E_{1/2}^{\text{red1}}$ = −0.77 V and $E_{1/2}^{\text{red2}}$ = −1.46 V). For comparison, NHPI has an oxidation potential E = 1.04 V, which means that the single electron transfer (SET) reaction could not occur between NHPI and Cu^{II}L. However, after adding NHPI (0.20 mM) to an argon-saturated CH₃CN solution of Cu^{II}L (0.10 mM) at 25 °C, the absorption band at 1167 nm disappeared, and the absorption intensity decreased at 435 nm. A new absorption



Table 2 Substrate scope^a

Entry	Substrate	Conv. ^b (%)	Selectivities ^b (%)
1		99	 >99
2		99	 >99
3		98	 97  3
4		48	 24  76
5		39	 98  2
6		47	 92  8
7		37	 83  17
8		76	 67  16  17
9 ^c		4	 24  76
10 ^c		34	 93  7
11 ^c		66	 66  34

^a Standard conditions: Substrate (20 mmol), Cu^{II}L (0.8 mol%), NHPI (4 mol%), CH₃CN (20 mL), O₂ (1 MPa), 70 °C, 7 h. ^b Determined by GC with naphthalene as the internal standard. ^c NHPI (10 mol%), 100 °C.

band appeared at 998 nm, and the color of the solution changed from black-green to yellow (Fig. 1A).

A blue-shift (1167 nm to 998 nm) occurred in the long-wavelength region, which indicated a decrease in the electron density of the conjugated system.³³ In addition, the characteristic absorption peak of the resulting solution was consistent with the directly synthesized Cu^{II}LH₂ and DFT computed UV-vis/NIR spectrum (Fig. S10†). The EPR spectrum of the resulting solution was also consistent with that of the directly synthesized Cu^{II}LH₂ (Fig. S11†). The presence of Cu^{II}LH₂ in the resulting solution was also indicated by high resolution mass spectrometry (Fig. S12†). Furthermore, when NHPI-d was used instead of NHPI (see Fig. S13† for the synthesis and characterization of NHPI-d), the CSI-MS (cold-spray ionization mass spectrometry) spectrum of the resulting solution exhibited a prominent ion peak at *m/z* = 579.3006, whose mass and isotope distribution patterns corresponded to Cu^{II}LD₂ (calcd *m/z* = 579.3002) (Fig. 1A, inset). In addition, EPR showed that the PINO radical (*A_N* = 4.6, *g* = 2.0073) was produced from homolysis of the O–H bond of NHPI (Fig. S14†).^{20a,34} These results demonstrate unambiguously that Cu^{II}L reacted with the hydrogen donor (NHPI) by H-atom transfers to form Cu^{II}LH₂.

Compared with 25 °C, the *in situ* generated Cu^{II}LH₂ shows a new absorption peak (464 nm) at 70 °C (Fig. 1B). This absorption is attributed to Cu(II) d–d bands and/or ligand to copper charge transfer transitions (LMCT).³² This led us to speculate whether this phenomenon was caused by structural changes of Cu^{II}LH₂ caused by temperature changes.

The ligand of Cu^{II}LH₂ is a closed shell and subsequently EPR-silent (radical silent). Surprisingly, when the reaction temperature was increased to 70 °C, the *in situ* generated Cu^{II}LH₂ in an argon atmosphere showed a typical *S* = 1/2 organic radical signal (*g* = 2.0043) with hyperfine coupling to two N donors (*I* = 1) and four H atoms (*I* = 1/2), which was not observed at room temperature (Fig. 1C). The EPR spectra of PINO may be covered due to the peak location (*g* = 2.0073) and total width (12 G).

Interestingly, the hyperfine splitting of the two N atoms (*A_{N(1)}* = 7.8 G, *A_{N(2)}* = 3.5 G) were unequal and nearly twofold, which means the two N atoms of the ligand have different effects on the spin center.³⁵ For organometallic radical complexes, when heteroatoms and spin centers are in different spatial positions, the values of hyperfine splitting are different (Table S2†).³⁶ Simultaneously, the small hyperfine splitting of the N atom indicates that the EPR signal is caused by the ligand-based delocalization of the π -electron.³⁷ Similar results were observed at 70 °C using directly synthesized Cu^{II}LH₂ (Fig. S15†). These results suggest that Cu^{II}LH₂ was distorted and led to a ligand-based radical at 70 °C.

The Cu K-edge XANES spectra of *in situ* generated Cu^{II}LH₂ show that the oxidation states of copper decreased (Fig. S16†).³⁸ Furthermore, the variable-temperature EPR experiment of *in situ* generated Cu^{II}LH₂ was conducted. Fig. 2 shows that the signal of Cu(II) is gradually enhanced with the decrease in temperature. The results indicated that some Cu(I) (3d¹⁰, EPR silent) species were present in the solution at 70 °C, but changed to Cu(II) with the decrease in temperature.^{11d,39} Based



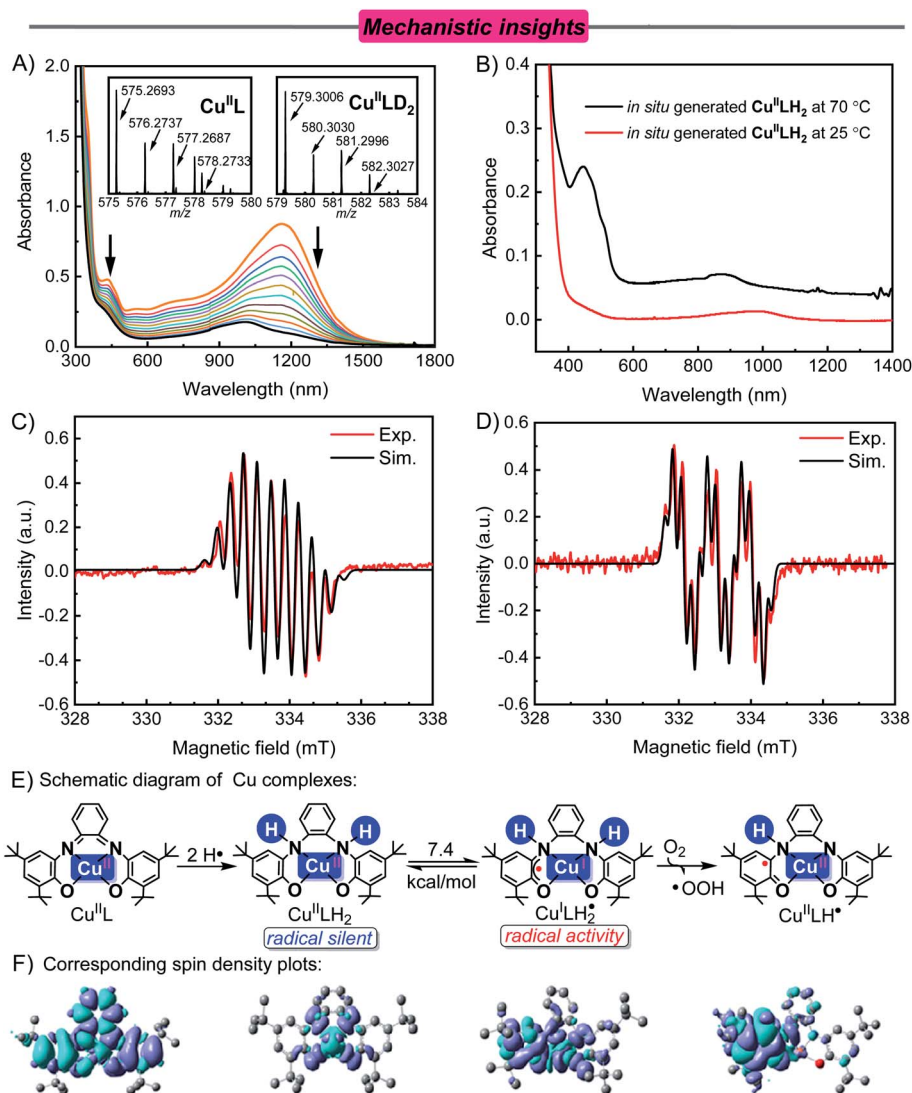


Fig. 1 (A) Electronic spectral changes observed in the reaction of $\text{Cu}^{\text{II}}\text{L}$ (0.1 mM) and NHPI (0.2 mM) in CH_3CN solvent under an argon atmosphere at 25 °C. Insets show the CSI-MS spectra of $\text{Cu}^{\text{II}}\text{L}$ and $\text{Cu}^{\text{II}}\text{LD}_2$. (B) Electronic spectra of *in situ* generated $\text{Cu}^{\text{II}}\text{LH}_2$ at 25 °C (red line) and 70 °C (black line) in CH_3CN solvent under an argon atmosphere. (C) Experimental (red) and simulated (black) X-band EPR spectra of $\text{Cu}^{\text{II}}\text{L}$ (0.10 mM) and NHPI (0.20 mM) in CH_3CN solvent under an argon atmosphere at 343 K. Frequency: 9.3615 GHz; Microwave power: 2.0 mW; modulation amplitude: 0.8 G. Parameters of simulated hyperfine splitting constants: $g_{\text{iso}} = 2.0043$ and $A_{\text{N,H,H,H,H,H}} = [7.8, 3.5, 3.5, 3.5, 3.5, 3.5]$ G. (D) X-band EPR spectra of *in situ* generated $\text{Cu}^{\text{II}}\text{LH}_2$ under an argon atmosphere followed by reaction with O_2 (1.0 MPa) in CH_3CN at 70 °C, $g_{\text{iso}} = 2.0043$ and $A_{\text{N,H,H,H,H,H}} = [9.5, 3.0, 2.0, 2.0, 2.0]$ G. (E) and (F) Schematic diagram and corresponding spin density plots of the Cu complex.

on the above experimental evidence, this phenomenon can be explained by the intramolecular redox reaction of $\text{Cu}^{\text{II}}\text{LH}_2$ at 70 °C, which results in the ligand-based unpaired π -electron and $\text{Cu}(\text{I})$.^{39c} For convenience, we express $\text{Cu}^{\text{II}}\text{LH}_2$ at 70 °C as a Cu^{I} -radical species, $\text{Cu}^{\text{I}}\text{LH}_2^\bullet$.

Subsequently, the cause of an intramolecular redox reaction in $\text{Cu}^{\text{II}}\text{LH}_2$ was explored. For electron transfer to occur between the ligand and the central Cu, the ligand's π orbital needs to overlap with the Cu $d_{x^2-y^2}$ orbital.^{39b} However, the optimized molecular structure of $\text{Cu}^{\text{II}}\text{LH}_2$ is still planar, and the electronic spectral peaks in the long-wavelength region primarily corresponded to ILCT (Fig. S17 and Table S3†). Obviously, intramolecular electron transfer cannot occur in the $\text{Cu}^{\text{II}}\text{LH}_2$ plane

structure because the ligand π orbital is perpendicular to the Cu $d_{x^2-y^2}$ orbital.

Therefore, the molecular structure of $\text{Cu}^{\text{II}}\text{LH}_2$ needs to be distorted to achieve antiferromagnetic coupling between the $d_{x^2-y^2}$ orbital of Cu(II) and the p_z orbital of the ligand. Due to the change in the N atom hybridization from sp^2 to sp^3 ($\text{Cu}^{\text{II}}\text{L}$ to $\text{Cu}^{\text{II}}\text{LH}_2$), the flexibility of $\text{Cu}^{\text{II}}\text{LH}_2$ increased.³⁰ This increases the possibility of changes in the ligand's spatial position. The speculated geometry of distorted $\text{Cu}^{\text{II}}\text{LH}_2$ ($\text{Cu}^{\text{I}}\text{LH}_2^\bullet$) is shown in Fig. S18.† The absorption spectrum obtained by excited state calculations is similar to that of *in situ* generated $\text{Cu}^{\text{II}}\text{LH}_2$ at 343 K (Fig. 1B), which proves that the conjecture is reasonable (Fig. S19†). The long-wavelength bands of $\text{Cu}^{\text{I}}\text{LH}_2^\bullet$ were attributed to ILCT and ligand-to-metal charge transfer (LMCT)



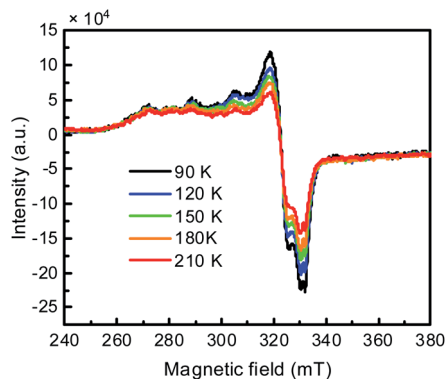


Fig. 2 Variable temperature X-band EPR spectra of *in situ* generated $\text{Cu}^{\text{II}}\text{LH}_2$. $\text{Cu}^{\text{II}}\text{L}$ (0.1 mM) and NHPI (0.2 mM) reacted in an argon atmosphere at 70 °C for 2 hours, and then were immediately placed in a 210 K environment for the EPR test.

transitions (Fig. S20 and Table S4†).¹⁶ In addition, the single-point energy calculations showed that the energy of $\text{Cu}^{\text{I}}\text{LH}_2^{\cdot}$ is 7.4 kcal mol^{−1} higher than that of $\text{Cu}^{\text{II}}\text{LH}_2$, which explained the different molecular structures caused by the temperature (Fig. 1E).

After the formation of $\text{Cu}^{\text{I}}\text{LH}_2^{\cdot}$, the addition of O_2 caused a new EPR signal ($g = 2.0043$, Fig. 1D). Combined with the hyperfine coupling to a N atom and four H atoms on the ligand, we assigned this EPR spectrum to the $\text{Cu}^{\text{II}}\text{LH}^{\cdot}$ radical (Fig. 1E). Furthermore, the spin density plot of $\text{Cu}^{\text{II}}\text{LH}^{\cdot}$ also showed that electrons were mainly concentrated in the conjugated system, which is consistent with the EPR data (Fig. 1E). Simultaneously, the EPR spectra of the HOO^{\cdot} radical ($A_{\text{N}} = 14.3$, $A_{\text{H}(\beta)} = 11.7$, $g = 2.0061$) was captured using DMPO (dimethyl pyridine N-oxide) as a trapping agent (Fig. S21†).⁴⁰ This indicates that an electron and a proton were transferred from $\text{Cu}^{\text{I}}\text{LH}_2^{\cdot}$ to O_2 . In contrast, O_2 cannot be activated at room temperature by $\text{Cu}^{\text{II}}\text{LH}_2$.

The reaction between $\text{Cu}^{\text{II}}\text{L}$ and NHPI involves the transfer of two electrons and two protons, and a stepwise thermochemical analysis was conducted. In the process, an electron and a proton of NHPI are transferred to $\text{Cu}^{\text{II}}\text{L}$ to form $\text{Cu}^{\text{II}}\text{LH}^{\cdot}$; the H^{\cdot} transfer in both stepwise electron transfer-proton transfer (ET-PT) ($\Delta G^{\circ} = 24.0$ kcal mol^{−1}) and PT-ET ($\Delta G^{\circ} = 65.6$ kcal mol^{−1}) processes involved high-energy intermediates (Scheme S1A†). In contrast, the PCET pathway ($\Delta G^{\circ} = 5.6$ kcal mol^{−1}, per Hess's Law) has obvious thermodynamic advantages.⁴¹ Similarly, the PCET pathway of the process, where an electron and a proton are transferred from NHPI to $\text{Cu}^{\text{II}}\text{LH}^{\cdot}$ to form $\text{Cu}^{\text{II}}\text{LH}_2$ ($\Delta G^{\circ} = 23.2$ kcal mol^{−1}), is energetically favorable (Scheme S1B†). Furthermore, the total energy ($\Delta G^{\circ} = 28.8$ kcal mol^{−1}) of the transfer of two electrons and protons from NHPI to $\text{Cu}^{\text{II}}\text{L}$ is relatively low, which indicates that PCET is a possible reaction pathway.

The radicals involved in oxidation were confirmed by the complete inhibition of oxidation by the addition of 10 mol% BHT (free radical scavenger) (Table 1, entry 10); therefore, the identification of reactive oxygen species was carried out by spin

trapping. During isobutane oxidation, the EPR spectrum of the $t\text{-Bu}$ -alkoxy radical captured by DMPO ($A_{\text{N}} = 14.5$, $A_{\text{H}(\beta)} = 10.5$, $g = 2.0062$) was detected.⁴² However, this signal was broadened, which resulted in other radical signals being covered (Fig. S22†). However, the adducts of DMPO and the $t\text{-Bu}$ -alkoxy radical ($m/z = 186.1494$) and DMPO and $^{\cdot}\text{OH}$ radicals ($m/z = 137.0857$) are identified by mass spectrometry (Fig. 3A, Fig. S23 and S24†). This indicates the presence of $^{\cdot}\text{OH}$ radicals in the reaction system.

H_2O_2 was also detected in the oxidation of isobutane by the probe reaction (Fig. S25†). In the contrast experiment, $\text{Cu}^{\text{II}}\text{L}$ efficiently decomposed H_2O_2 to produce $^{\cdot}\text{OH}$ radicals (Fig. S26†). To further confirm the existence of $^{\cdot}\text{OH}$ radicals in the reaction system, Fig. S27A† shows the EPR spectrum of the reaction solution using BMPO (5-*tert*-butoxycarbonyl 5-methyl-1-pyrroline N-oxide)⁴³ as a capture agent, which is consistent with the $^{\cdot}\text{OH}$ radical generated by the Fenton reaction captured by BMPO (Fig. S27B†). In addition, $^{\cdot}\text{OH}$ radical can be quenched by ethanol.⁴⁴ The reaction solution of oxidation of isobutane was quenched with ethanol, and the $\text{C}_2\text{H}_4\text{OH}$ radicals were captured by DMPO (Fig. S28A and S28B†). This phenomenon was also consistent with that of the Fenton reaction (Fig. S28C†). These results indicated that an $^{\cdot}\text{OH}$ radical is the oxygen species in the reaction process.

Nitroxyl radicals are widely used in the aerobic oxidation of C–H bonds, but they have some limitations such as a long initiation period, a short existence time and self-decomposition.^{20d} In the $\text{Cu}^{\text{II}}\text{L}$ –NHPI catalytic system, time-dependent experiments were conducted to investigate the PINO radical by EPR. The PINO radicals are rapidly produced and accumulated to maximum concentrations within 60 min, which are attributed to the bionic catalyst $\text{Cu}^{\text{II}}\text{L}$ superior hydrogen extraction ability (Fig. 3B). Furthermore, the concentration of the PINO radical decreased slowly, lasting up to 480 minutes (Fig. 3B). This indicated the existence of persistent PINO radicals in the $\text{Cu}^{\text{II}}\text{L}$ –NHPI system, which is desirable for efficient reactions.^{23b,45} Combined with the time curves of isobutane oxidation, the initiation period and rapid reaction phase were synchronized with a change in the PINO radical (Fig. 3B). This further illustrates the importance of the PINO radical. In addition, when isobutane was replaced with cyclohexane- d_{12} , the recovered NHPI contained deuterium products NHPI- d (Fig. S29†). This phenomenon suggests that PINO radicals activate substrates by extracting a hydrogen atom from the C–H bond of the substrate.^{20e}

To obtain direct evidence about the carbon-centered radical, radical capture experiments were performed in an Ar atmosphere. As shown in Fig. 3C, the spin-trap experiments with DMPO revealed the presence of a carbon-centered *tert*-butyl radical (Sim-C, $A_{\text{N}} = 14.3$, $A_{\text{H}(\beta)} = 21.8$, $g = 2.0048$) and a nitrogen-centered radical (Sim-N, $A_{\text{N}1} = 14.1$, $A_{\text{N}2} = 2.4$, $A_{\text{H}(\beta)} = 12.6$, $g = 2.0050$).⁴² To our knowledge, this is also the first report of the capture of a *tert*-butyl radical (C4) during homogeneous catalytic oxidation. However, this signal was unstable due to its high activity. When isobutane was replaced by cyclohexane, we captured $^{\cdot}\text{C}_6\text{H}_{11}$, $\text{C}_6\text{H}_{11}\text{O}^{\cdot}$, and $\text{C}_6\text{H}_{11}\text{OO}^{\cdot}$ radicals under an O_2 atmosphere (Fig. S30†). In addition, 1-



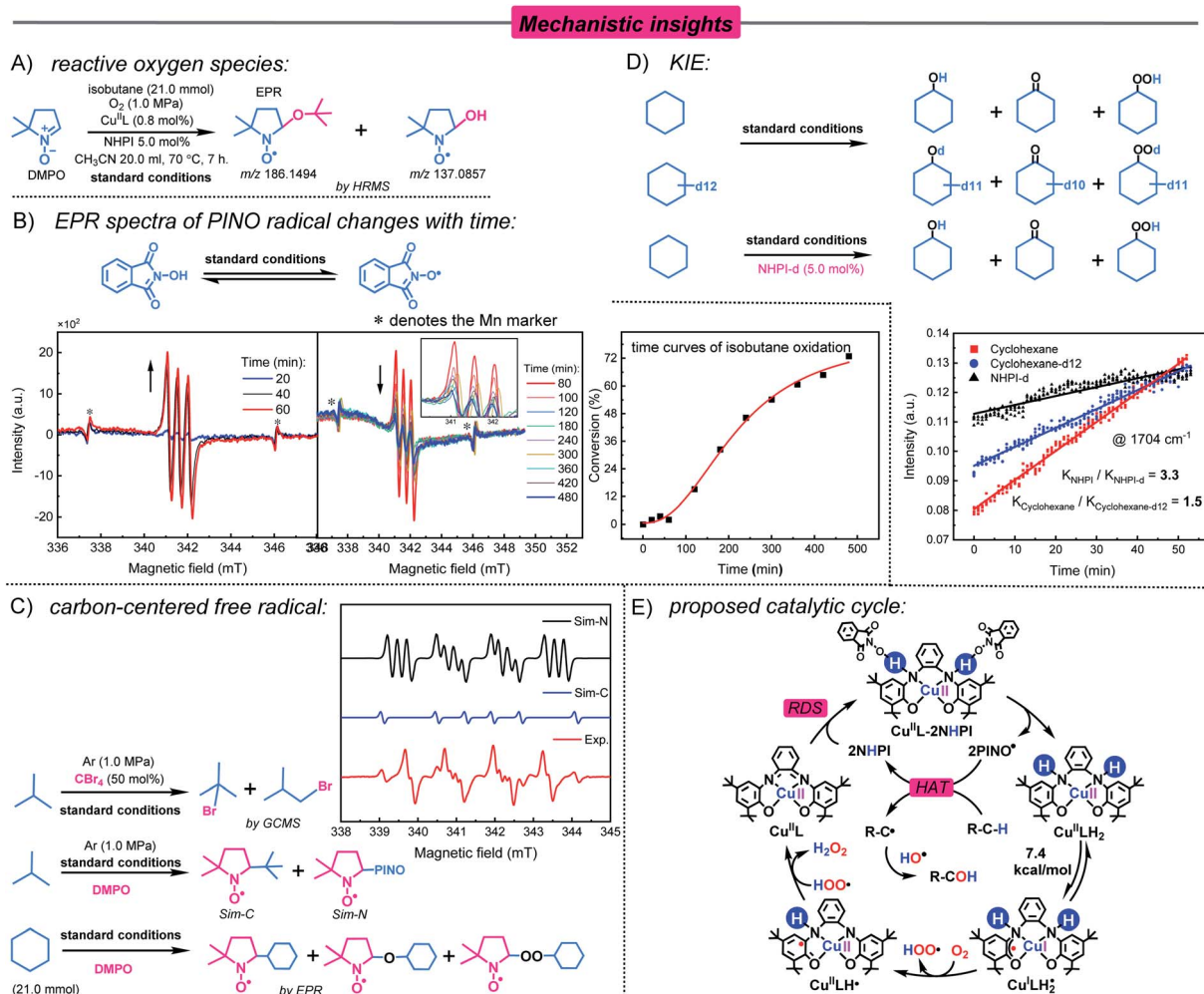


Fig. 3 Mechanistic studies for $\text{Cu}^{\text{II}}\text{L}$ -NHPI catalyzed aerobic oxidation. (A) Reactive oxygen species. (B) EPR spectra of PINO radical changes with time and the time curves of the isobutane oxidation reaction. Reaction condition: isobutane (21.0 mmol), $\text{Cu}^{\text{II}}\text{L}$ (0.8 mol%), NHPI (4.0 mol%), solvent (CH_3CN , 20.0 mL) and O_2 (1.0 MPa) 70 °C. (C) Carbon-centered free radical. Experimental and simulated EPR spectra of the mixture of isobutane (21.0 mmol), $\text{Cu}^{\text{II}}\text{L}$ (0.8 mol%), and NHPI (4.0 mol%) in CH_3CN (20.0 mL) under argon (1.0 MPa) at 70 °C. DMPO was used as a spin trapping agent. Simulation parameters (Sim-N, $A_{\text{N1}} = 14.1$, $A_{\text{N2}} = 2.4$, $A_{\text{H(B)}} = 12.6$, $g = 2.0050$; Sim-C, $A_{\text{N}} = 14.3$, $A_{\text{H(B)}} = 21.8$, $g = 2.0048$). (D) KIE experiment. *In situ* infrared spectra showing the variations in the peak at 1704 cm^{-1} . Reaction conditions: cyclohexane/cyclohexane- d_{12} (21.0 mmol), $\text{Cu}^{\text{II}}\text{L}$ (0.8 mol%), NHPI/NHPI-d (4.0 mol%), and O_2 (1.0 MPa) in CH_2Cl_2 (20.0 mL) at 100 °C. (E) Proposed catalytic cycle.

bromo-2-methylpropane and 2-bromo-2-methylpropane were identified by adding 50 mol% CBr_4 (Fig. 3C). This indicates that in the $\text{Cu}^{\text{II}}\text{L}$ -NHPI system, C-H bond activation mainly occurred *via* the formation of a carbon-centered radical.

According to previous studies, the C-H activation approach *via* the HAT process was likely to be involved in the rate-determining step (RDS).⁴⁶ The kinetic isotope effect (KIE) experiment was carried out by *in situ* infrared spectroscopy. Cyclohexane oxidation was used as a model reaction. The reaction kinetics was studied by monitoring the absorption peak of the oxidation product cyclohexanone at 1704 cm^{-1} ($\text{C}=\text{O}$ bond) over time (Fig. 3D and S31†). A KIE value of 1.5 ($K_{\text{H}}/K_{\text{D}}$) was obtained for the oxidation of cyclohexane and cyclohexane- d_{12} by the $\text{Cu}^{\text{II}}\text{L}$ -NHPI system. Thus, the C-H activation step should not be the rate-determining step.⁴⁷ However, when NHPI-d was used for oxidation, the value of KIE was 3.3, which

indicates that the activation of NHPI is the rate-determining step.⁴⁸

Based on the experimental results and thermochemical calculations, a possible reaction pathway was outlined (Fig. 3E). First, $\text{Cu}^{\text{II}}\text{L}$ reacts with NHPI (electron and proton donor) through two successive PCET processes to form $\text{Cu}^{\text{II}}\text{LH}_2$. This process may be the rate-determining step of the reaction through the KIE experiment. Subsequently, $\text{Cu}^{\text{II}}\text{LH}_2$ is converted to a Cu^I-radical species $\text{Cu}^{\text{I}}\text{LH}_2^{\cdot}$ through an intramolecular redox reaction at 70 °C. $\text{Cu}^{\text{I}}\text{LH}_2^{\cdot}$ is a highly reactive radical intermediate that reacts with O_2 to produce $\text{Cu}^{\text{II}}\text{LH}^{\cdot}$ and HOO^{\cdot} radicals. Next, the catalytic cycle returns to the starting point, with the formation of H_2O_2 by the transfer of electrons and proton from $\text{Cu}^{\text{II}}\text{LH}^{\cdot}$ to HOO^{\cdot} . H_2O_2 is rapidly decomposed into reactive oxygen species $^{\cdot}\text{OH}$ under the reaction conditions. Activation of O_2 by the $\text{Cu}^{\text{II}}\text{L}$ -NHPI system is similar to the

oxidation of alcohol by galactose oxidase. More importantly, this process is also accompanied by the production of a persistent PINO radical for substrate C–H bond activation by HAT. Subsequently, the carbon-centered radical reacts with reactive oxygen species in the reaction system to generate oxidation products.

Conclusions

In summary, we developed the protocol for C–sp(3)–H efficient catalytic aerobic oxidation under mild conditions based on a GOase model compound $\text{Cu}^{\text{II}}\text{L}$ and NHPI. In particular, the $\text{Cu}^{\text{II}}\text{L}$ –NHPI system showed excellent performance for the oxidation of light alkanes (C2–C4). $\text{Cu}^{\text{II}}\text{L}$ can activate NHPI efficiently to generate PINO radicals and $\text{Cu}^{\text{II}}\text{LH}_2$ through the PCET pathway. Based on the EPR tests and theoretical calculations, the intramolecular redox process of $\text{Cu}^{\text{II}}\text{LH}_2$ has been proved. Throughout the catalytic cycle, O_2 is reduced to its active form and the C–sp(3)–H bond of the substrate is converted to a highly active carbon-centered radical by PINO through the HAT pathway. Kinetic experiments showed the activation of NHPI was the rate-determining step. Meanwhile, the generation of PINO radicals was demonstrated by time-resolved EPR tests. It indicated the persistent radicals played an important role in oxidation.

Data availability

Data for this paper, including reaction screening and optimization experiments, detailed experimental procedures, spectral data, and computational study details, are provided in the ESI.†

Author contributions

X. L. and X. Z. developed the concept, designed these experiments, analyzed the experimental data and wrote the paper. J. S. analyzed the EPR experimental data. H. Y., J. H., C. X., Y. H., Q. H., D. X., and C. X. contributed to catalyst synthesis, catalytic experiments and analyzed the experimental data. X. Z. and H. J. directed the project. All authors discussed the results and provided comments during the manuscript preparation.

Conflicts of interest

There are no conflicts to declare.

Acknowledgements

This work was financially supported by the National Key Research and Development Program of China (2020YFA0210900), the National Natural Science Foundation of China (No. 21938001 and 21878344), the Guangdong Provincial Key R&D Programme (2019B110206002), and the Local Innovative and Research Teams Project of the Guangdong Pearl River Talents Program (2017BT01C102).

Notes and references

- For selected and recent reviews on oxidation reactions, see: (a) Y. Liang, J. Wei, X. Qiu and N. Jiao, *Chem. Rev.*, 2018, **118**, 4912–4945; (b) C. Tang, X. Qiu, Z. Cheng and N. Jiao, *Chem. Soc. Rev.*, 2021, **50**, 8067–8101; (c) E. Roduner, W. Kaim, B. Sarkar, V. B. Urlacher, J. Pleiss, R. Glaeser, W. D. Einicke, G. A. Sprenger, U. Beifuss, E. Klemm, C. Liebner, H. Hieronymus, S. F. Hsu, B. Plietker and S. Laschat, *ChemCatChem*, 2013, **5**, 82–112.
- For selected reviews and studies on C–H functionalization and radical C–H activation, see: (a) H. Sterckx, B. Morel and B. U. W. Maes, *Angew. Chem., Int. Ed.*, 2019, **58**, 7946–7970; (b) Y. Qin, L. Zhu and S. Luo, *Chem. Rev.*, 2017, **117**, 9433–9520; (c) Y. Liu, H. Yi and A. Lei, *Chin. J. Chem.*, 2018, **36**, 692–697; (d) H. Yi, G. Zhang, H. Wang, Z. Huang, J. Wang, A. K. Singh and A. Lei, *Chem. Rev.*, 2017, **117**, 9016–9085; (e) Y. F. Liang and N. Jiao, *Acc. Chem. Res.*, 2017, **50**, 1640–1653.
- J. T. Grant, J. M. Venegas, W. P. McDermott and I. Hermans, *Chem. Rev.*, 2018, **118**, 2769–2815.
- For recent reviews on homogeneous catalytic oxidation, see: (a) Z. Zheng, X. Ma, X. Cheng, K. Zhao, K. Gutman, T. Li and L. Zhang, *Chem. Rev.*, 2021, **121**, 8979–9038; (b) L. Marais, H. C. M. Vosloo and A. J. Swarts, *Coord. Chem. Rev.*, 2021, **440**, 213958.
- J. C. Lewis, P. S. Coelho and F. H. Arnold, *Chem. Soc. Rev.*, 2011, **40**, 2003–2021.
- S. R. Docherty, L. Rochlitz, P. A. Payard and C. Coperet, *Chem. Soc. Rev.*, 2021, **50**, 5806–5822.
- For the leading references, see: (a) J. Sheng, B. Yan, W. D. Lu, B. Qiu, X. Q. Gao, D. Wang and A. H. Lu, *Chem. Soc. Rev.*, 2021, **50**, 1438–1468; (b) Y. Wang, P. Hu, J. Yang, Y. A. Zhu and D. Chen, *Chem. Soc. Rev.*, 2021, **50**, 4299–4358.
- L. Xiong and J. Tang, *Adv. Energy Mater.*, 2021, **11**, 2003216.
- Y. Kawamata, M. Yan, Z. Liu, D. H. Bao, J. Chen, J. T. Starr and P. S. Baran, *J. Am. Chem. Soc.*, 2017, **139**, 7448–7451.
- M. S. A. S. Shah, C. Oh, H. Park, Y. J. Hwang, M. Ma and J. H. Park, *Adv. Sci.*, 2020, **7**, 2001946.
- For reviews and studies on galactose oxidase, see: (a) J. Li, I. Davis, W. P. Griffith and A. Liu, *J. Am. Chem. Soc.*, 2020, **142**, 18753–18757; (b) E. I. Solomon, D. E. Heppner, E. M. Johnston, J. W. Ginsbach, J. Cirera, M. Qayyum, M. T. Kieber-Emmons, C. H. Kjaergaard, R. G. Hadt and L. Tian, *Chem. Rev.*, 2014, **114**, 3659–3853; (c) J. M. Hoover and S. S. Stahl, *J. Am. Chem. Soc.*, 2011, **133**, 16901–16910; (d) J. M. Hoover, B. L. Ryland and S. S. Stahl, *J. Am. Chem. Soc.*, 2013, **135**, 2357–2367.
- For selected reviews on the structure of galactose oxidase, see: (a) W. R. Birmingham and N. J. Turner, *ACS Catal.*, 2018, **8**, 4025–4032; (b) J. W. Whittaker, *Chem. Rev.*, 2003, **103**, 2347–2363.
- For the proposed mechanism for the oxidation of alcohols to aldehydes by GOase, see: (a) P. Chaudhuri, M. Hess, T. Weyhermuller and K. Wieghardt, *Angew. Chem., Int. Ed.*,



- 1999, **38**, 1095–1098; (b) H. Oshita and Y. Shimazaki, *Chem.–Eur. J.*, 2020, **26**, 8324–8340.
- 14 W. Kaim and B. Schwederski, *Coord. Chem. Rev.*, 2010, **254**, 1580–1588.
- 15 N. Kitajima, K. Whang, Y. Moro-oka, A. Uchida and Y. Sasada, *J. Chem. Soc., Chem. Commun.*, 1986, 1504–1505.
- 16 (a) Y. Wang, J. L. Dubois, B. Hedman, K. O. Hodgson and T. D. P. Stack, *Science*, 1998, **279**, 537–540; (b) I. L. Fedushkin, O. V. Maslova, A. G. Morozov, S. Dechert, S. Demeshko and F. Meyer, *Angew. Chem., Int. Ed.*, 2012, **51**, 10584–10587; (c) T. Glaser, M. Heidemeler, R. Frohlich, P. Hildebrandt, E. Bothe and E. Bill, *Inorg. Chem.*, 2005, **44**, 5467–5482.
- 17 E. Saint-Aman, S. Menage, J. L. Pierre, E. Defrancq and G. Gellon, *New J. Chem.*, 1998, **22**, 393–394.
- 18 P. Chaudhuri, M. Hess, J. Muller, K. Hildenbrand, E. Bill, T. Weyhermuller and K. Wieghardt, *J. Am. Chem. Soc.*, 1999, **121**, 9599–9610.
- 19 (a) H. Chen, L. Wang, S. Xu, X. Liu, Q. He, L. Song and H. Ji, *ACS Catal.*, 2021, **11**, 6810–6815; (b) P. Gandeepan, T. Mueller, D. Zell, G. Cera, S. Warratz and L. Ackermann, *Chem. Rev.*, 2019, **119**, 2192–2452.
- 20 For selected examples with *N*-oxyl radicals as catalysts, see: (a) J. E. Nutting, M. Rafiee and S. S. Stahl, *Chem. Rev.*, 2018, **118**, 4834–4885; (b) S. Tsujimoto, T. Iwahama, S. Sakaguchi and Y. Ishii, *Chem. Commun.*, 2001, 2352–2353; (c) Y. Amaoka, M. Nagatomo and M. Inoue, *Org. Lett.*, 2013, **15**, 2160–2163; (d) T. Yoshii, S. Tsuzuki, S. Sakurai, R. Sakamoto, J. Jiang, M. Hatanaka, A. Matsumoto and K. Maruoka, *Chem. Sci.*, 2020, **11**, 5772–5778; (e) M. Petroselli, L. Melone, M. Cametti and C. Punta, *Chem.–Eur. J.*, 2017, **23**, 10616–10625.
- 21 S. Sakaguchi, S. Kato, T. Iwahama and Y. Ishii, *Bull. Chem. Soc. Jpn.*, 1998, **71**, 1237–1240.
- 22 Y. Yan, P. Feng, Q. Z. Zheng, Y. F. Liang, J. F. Lu, Y. Cui and N. Jiao, *Angew. Chem., Int. Ed.*, 2013, **52**, 5827–5831.
- 23 (a) E. Baciocchi, M. F. Gerini and O. Lanzalunga, *J. Org. Chem.*, 2004, **69**, 8963–8966; (b) N. Koshino, B. Saha and J. H. Espenson, *J. Org. Chem.*, 2003, **68**, 9364–9370.
- 24 Y. Mo and K. F. Jensen, *Chem.–Eur. J.*, 2018, **24**, 10260–10265.
- 25 C. Zhang, Z. Huang, J. Lu, N. Luo and F. Wang, *J. Am. Chem. Soc.*, 2018, **140**, 2032–2035.
- 26 J. R. Wang, L. Liu, Y. F. Wang, Y. Zhang, W. Deng and Q. X. Guo, *Tetrahedron Lett.*, 2005, **46**, 4647–4651.
- 27 E. Gaster, S. Kozuch and D. Pappo, *Angew. Chem., Int. Ed.*, 2017, **56**, 5912–5915.
- 28 S. J. Blanksby and G. B. Ellison, *Acc. Chem. Res.*, 2003, **36**, 255–263.
- 29 (a) Y. Liu, S. G. Resch, I. Klawitter, G. E. Cutsail, S. Demeshko, S. Dechert, F. E. Kuehn, S. DeBeer and F. Meyer, *Angew. Chem., Int. Ed.*, 2020, **59**, 5696–5705; (b) B. M. Armstrong, R. I. Sayler, B. H. Shupe, T. A. Stich, R. D. Britt and A. K. Franz, *ACS Catal.*, 2019, **9**, 1224–1230.
- 30 S. Ghorai, A. Sarmah, R. K. Roy, A. Tiwari and C. Mukherjee, *Inorg. Chem.*, 2016, **55**, 1370–1380.
- 31 A. Vogler and H. Kunkely, *Coord. Chem. Rev.*, 2000, **200**, 991–1008.
- 32 P. Verma, J. Weir, L. Mirica and T. D. P. Stack, *Inorg. Chem.*, 2011, **50**, 9816–9825.
- 33 A. Rana, Y. –M. Lee, X. Li, R. Cao, S. Fukuzumi and W. Nam, *ACS Catal.*, 2021, **11**, 3073–3083.
- 34 L. Wang, Y. Zhang, R. Du, H. Yuan, Y. Wang, J. Yao and H. Li, *Chemcatchem*, 2019, **11**, 2260–2264.
- 35 (a) P. Chaudhuri, M. Hess, J. Müller, K. Hildenbrand, E. Bill, T. Weyhermüller and K. Wieghardt, *J. Am. Chem. Soc.*, 1999, **121**, 9599–9610; (b) C. L. Wagner, G. Herrera, Q. Lin, C. T. Hu and T. Diao, *J. Am. Chem. Soc.*, 2021, **143**, 5295–5300.
- 36 S. Roy, B. Dittrich, T. Mondal, D. Koley, A. C. Stueckl, B. Schwederski, W. Kaim, M. John, S. K. Vasa, R. Linser and H. W. Roesky, *J. Am. Chem. Soc.*, 2015, **137**, 6180–6183.
- 37 (a) K. C. Mondal, H. W. Roesky, A. C. Stueckl, F. Ehret, W. Kaim, B. Dittrich, B. Maity and D. Koley, *Angew. Chem., Int. Ed.*, 2013, **52**, 11804–11807; (b) B. Kirste, *Magn. Reson. Chem.*, 2016, **54**, 835–841.
- 38 E. Borfecchia, P. Beato, S. Svelle, U. Olsbye, C. Lamberti and S. Bordiga, *Chem. Soc. Rev.*, 2018, **47**, 8097–8133.
- 39 (a) K. Rajabimoghadam, Y. Darwish, U. Bashir, D. Pitman, S. Eichelberger, M. A. Siegler, M. Swart and I. Garcia–Bosch, *J. Am. Chem. Soc.*, 2018, **140**, 16625–16634; (b) W. Kaim, *Dalton Trans.*, 2003, 761–768; (c) J. Rall, M. Wanner, M. Albrecht, F. M. Hornung and W. Kaim, *Chem.–Eur. J.*, 1999, **5**, 2802–2809.
- 40 J. M. Fontmorin, R. C. B. Castillo, W. Z. Tang and M. Sillanpaa, *Water Res.*, 2016, **99**, 24–32.
- 41 R. Tyburski, T. Liu, S. D. Glover and L. Hammarstrom, *J. Am. Chem. Soc.*, 2021, **143**, 560–576.
- 42 S. Wu, Y. He, C. Wang, C. Zhu, J. Shi, Z. Chen, Y. Wan, F. Hao, W. Xiong, P. Liu and H. Luo, *ACS Appl. Mater.*, 2020, **12**, 26733–26745.
- 43 J. Chang, R. D. Taylor, R. A. Davidson, A. Sharmah and T. Guo, *J. Phys. Chem. A*, 2016, **120**, 2815–2823.
- 44 (a) R. C. Kukreja, E. Okabe, G. M. Schrier and M. L. Hess, *Arch. Biochem. Biophys.*, 1988, **261**, 447–457; (b) M. B. Yim, P. B. Chock and E. R. Stadtman, *Proc. Natl. Acad. Sci. U. S. A.*, 1990, **87**, 5006–5010.
- 45 (a) J. Lalevee, N. Blanchard, M. El–Roz, X. Allonas and J. P. Fouassier, *Macromolecules*, 2008, **41**, 2347–2352; (b) D. Leifert and A. Studer, *Angew. Chem., Int. Ed.*, 2020, **59**, 74–108.
- 46 X. Hu, G. Zhang, F. Bu, L. Nie and A. Lei, *ACS Catal.*, 2018, **8**, 9370–9375.
- 47 Y. Liu, B. Shi, Z. Liu, R. Gao, C. Huang, H. Alhumade, S. Wang, X. Qi and A. Lei, *J. Am. Chem. Soc.*, 2021, **143**, 20863–20872.
- 48 (a) C. Y. Huang, J. Li, W. Liu and C. J. Li, *Chem. Sci.*, 2019, **10**, 5018–5024; (b) A. P. Antonchick and L. Burgmann, *Angew. Chem., Int. Ed.*, 2013, **52**, 3267–3271.

